Chinese Chemical Letters 37 (2026) 112016

Contents lists available at ScienceDirect

Chinese Chemical Letters

journal homepage: www.elsevier.com/locate/cclet

Engineering macrocyclic nanoconfinement in covalent networks *via* internal charge redistribution for defined photocatalysis and adsorption

Meng-Hao Li[a,1], Hui Hui[a,1], Yan Wang[a,*], Weiwei Huan[b,*], Ying-Wei Yang[a,*]

[a] *International Joint Research Laboratory of Nano-Micro Architecture Chemistry, College of Chemistry, Jilin University, Changchun 130012, China*
[b] *Zhejiang Provincial Key Laboratory of Chemical Utilization of Forestry Biomass, College of Chemistry and Materials Engineering, Zhejiang A&F University, Hangzhou 311300, China*

ARTICLE INFO

Article history:
Received 15 August 2025
Revised 13 October 2025
Accepted 22 October 2025
Available online 24 October 2025

Keywords:
Supramolecular chemistry
Pillararenes
Porous materials
Photocatalysis
Porous organic polymers

ABSTRACT

Mimicking natural energy conversion processes, the pursuit of metal-free porous organic polymers (POPs) as heterogeneous catalysts for photocatalytic oxidation is a major driving force in materials science, seeking to achieve high-performance artificial photochemical systems. In this work, we report the bottom-up synthesis of a hydrazone-linked pillararene POP in its keto form. The inherent pillararene cavities provide a unique nanoconfinement environment, enabling effective substrate recognition and electron enrichment, thereby facilitating sensitive photo-response and efficient photoenergy-to-chemical energy conversion for photocatalytic oxidation coupling of primary amines (up to 99% conversion). Crucially, the framework's tautomeric state is precisely modulated *via* an irreversible keto-to-enol conversion using sodium borohydride reduction. This controlled tautomerism permanently tunes the nanoconfinement microenvironment, amplifying the polymer's electron-rich character and optimizing pore electrostatic properties. Leveraging this tunable nanoconfinement, the resulting enol form framework achieves highly efficient adsorption of cationic pollutants (up to 95% removal for Rhodamine B). This work establishes tautomerism as a chemical tool to engineer nanoconfinement in macrocycle-based POPs, expanding the toolbox for advanced porous materials with tailored functionalities for diverse applications like photocatalysis and adsorption.

© 2026 Published by Elsevier B.V. on behalf of Chinese Chemical Society and Institute of Materia Medica, Chinese Academy of Medical Sciences.

Supramolecular macrocycles possessing well-defined cavities, such as crown ethers [1], cyclodextrins [2], calixarenes [3], and pillararenes [4,5], serve as platforms for a diverse range of applications, including molecular machines, adsorption, sensing, catalysis, and drug delivery [6–11]. This stems from their inherent host–guest recognition, tunable self-assembly behavior, and dynamic responsiveness in solution. Among macrocyclic arenes, pillararenes have emerged as a prominent class of host compounds in supramolecular chemistry [12–14]. Their rigid, pillar-shaped architecture, coupled with symmetrical frameworks and electron-rich aromatic cavities, endows them with distinctive physicochemical properties and remarkable host–guest recognition capabilities. However, a persistent challenge in utilizing these macrocycles, particularly in the solid states, is the hindered mass transport to and from their interior, often resulting from close molecular packing [15–17]. Consequently, innovative strategies are needed to enhance the functionality of these macrocycles and overcome the application barriers imposed by such pore blockage. Promisingly, well-defined polymers synthesized *via* bottom-up approaches offer a viable avenue to address this limitation [18–21].

Within the diverse landscape of polymers, porous organic polymers (POPs) represent a compelling platform for designing advanced multifunctional materials [22–26]. Their pre-organized and modular architectures enable the controlled positioning of functional groups, providing a key handle for property customization. The bottom-up design of POPs, proceeding from molecular monomers to extended frameworks, is often guided by two widely adopted principles: (1) Pre-design of building blocks is crucial for endowing the material with specific functionalities, thereby establishing structure–function relationships that govern its application [27–31]; (2) Rational modulation of linker units is essential for optimizing and amplifying the physicochemical properties of the resulting framework [32–39]. These linkers, through intrinsic design

* Corresponding authors.
E-mail addresses: wangy2011@jlu.edu.cn (Y. Wang), huanweiwei@zafu.edu.cn (W. Huan), ywyang@jlu.edu.cn (Y.-W. Yang).
[1] These authors contributed equally to this work.

https://doi.org/10.1016/j.cclet.2025.112016
1001-8417/© 2026 Published by Elsevier B.V. on behalf of Chinese Chemical Society and Institute of Materia Medica, Chinese Academy of Medical Sciences.

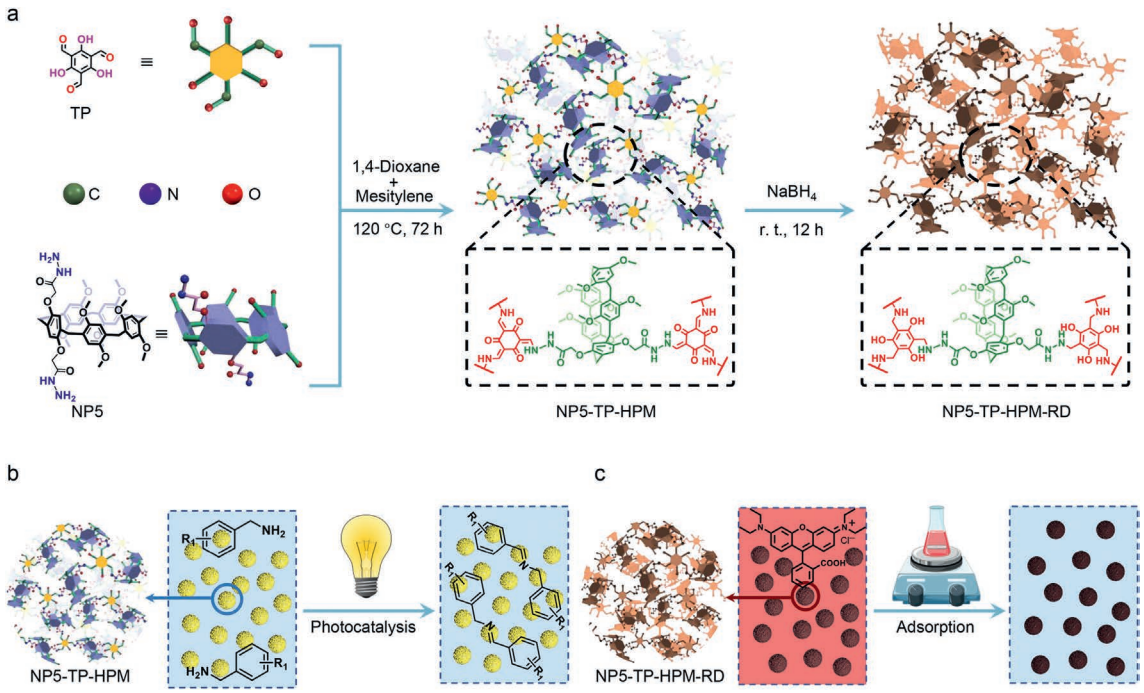


Fig. 1. (a) Synthetic routes of NP5-TP-HPM and NPH-TF-HPM-RD. (b) Schematic diagram of the photocatalytic oxidation coupling of benzylamine by NP5-TP-HPM. (c) Schematic diagram of RhB adsorption on NP5-TP-HPM-RD.

or post-synthetic modification, synergistically reinforce structural rigidity and topology while precisely tuning the pore environment, encompassing pore size distribution, specific surface area, and pore surface chemistry. As a result, this precise pore engineering, combined with the pre-organization and microenvironmental cooperativity of confined functional groups, facilitates efficient guest uptake and enables the directional enhancement of functional group activity [19,31,40].

Against this backdrop, the incorporation of macrocyclic arenes, especially pillararenes, into POP structures emerges as a highly promising strategy for constructing advanced functional materials [18,19,41–45]. This approach combines the inherent advantages of network polymers, such as permanent porosity, exceptional structural stability (acid, base, and thermal resistance), and excellent recyclability, with the distinct features and rich supramolecular functions of pillararenes, including their electron-rich cavities, facile functionalization, and potent molecular/ion recognition abilities [17,42–44,46,47]. Following the initial synthesis of a pillar[5]arene-based conjugated microporous polymer by Coskun and coworkers [48], numerous highly active pillararene-containing POPs have been developed for diverse applications, ranging from gas adsorption and separation to sensing and catalysis [17,42,46,49,50]. Despite these advancements, precisely controlling the microenvironment within pillararene-based covalent frameworks to fine-tune their functionalities remains a challenge. While current strategies primarily rely on pre-design of monomers or post-synthetic modification of framework connectivity, a molecular-level precise control over the cavity environment, particularly for regulating host-guest interactions and charge transfer processes, is still largely underexplored. Accordingly, the rational design of cavity-directed monomers for constructing frameworks with alternating pillararene units and covalent linkages, to achieve synergistic functions, remains a significant research endeavor.

Guided by these principles, we implemented a tautomerism-facilitated chemical-editing strategy within a hydrazone-linked pillararene POP. An irreversible C=N reduction to C–N introduces phenolic hydroxyl groups, permanently reshaping the network conjugation and pore-surface chemistry (Fig. 1a), and thereby directing cavity-internal charge distribution and host–guest affinity. This resulting confinement of the cavity environment enables precise microenvironmental control, affording a switch between robust visible-light photocatalytic oxidation and enhanced binding of cationic pollutants, thereby demonstrating the multifunctionality inherent in pillararene-based networks. Initially, the hydrazone-linked pillararene framework synthesized with a predominant β-ketoenamine form, termed NP5-TP-HPM, exhibit pronounced photoactivity. The materials facilitate efficient photoelectron transfer and the generation of reactive oxygen species (ROS), coupled with an inherent affinity for electron-deficient substrates/intermediates. This remarkable synergy facilitates the highly efficient photocatalytic oxidative coupling of benzylamine derivatives into imines (Fig. 1b) by exploiting host–guest interactions and cavity confinement, resulting in a maximum conversion of 99%. Intriguingly, by irreversibly stabilizing the enol form of the pillararene-based framework (NP5-TP-HPM-RD) *via* a simple post-synthetic reduction strategy, we successfully optimize the unique properties of the electron-rich pillararene cavity, significantly enhancing the adsorption capacity for cationic pollutants such as Rhodamine B (RhB) (Fig. 1c). Considering the broad relevance of photocatalytic oxidation for chemical synthesis and environmental remediation, as well as the environmental concerns associated with cationic dyes, the multifunctional nature of these pillararene-based frameworks, enabled by this molecular-level control strategy, underscores their significant potential for applications in catalysis, separation, and environmental remediation.

A hydrazone-linked pillar[5]arene-based framework, denoted NP5-TP-HPM, was synthesized *via* solvothermal condensation of 2,4,6-triformylphloroglucinol (TP) and the hydrazide-modified pillar[5]arene (NP5), following a reported protocol with slight modifications (Fig. 1) [26,39,51,52]. Subsequent reduction of NP5-TP-HPM with $NaBH_4$ at room temperature for 12 h afforded the flexible derivative, NP5-TP-HPM-RD. Preliminary confirmation of successful synthesis was obtained through Fourier transform infrared (FT-IR) spectroscopy (Fig. S1 in Supporting information). The

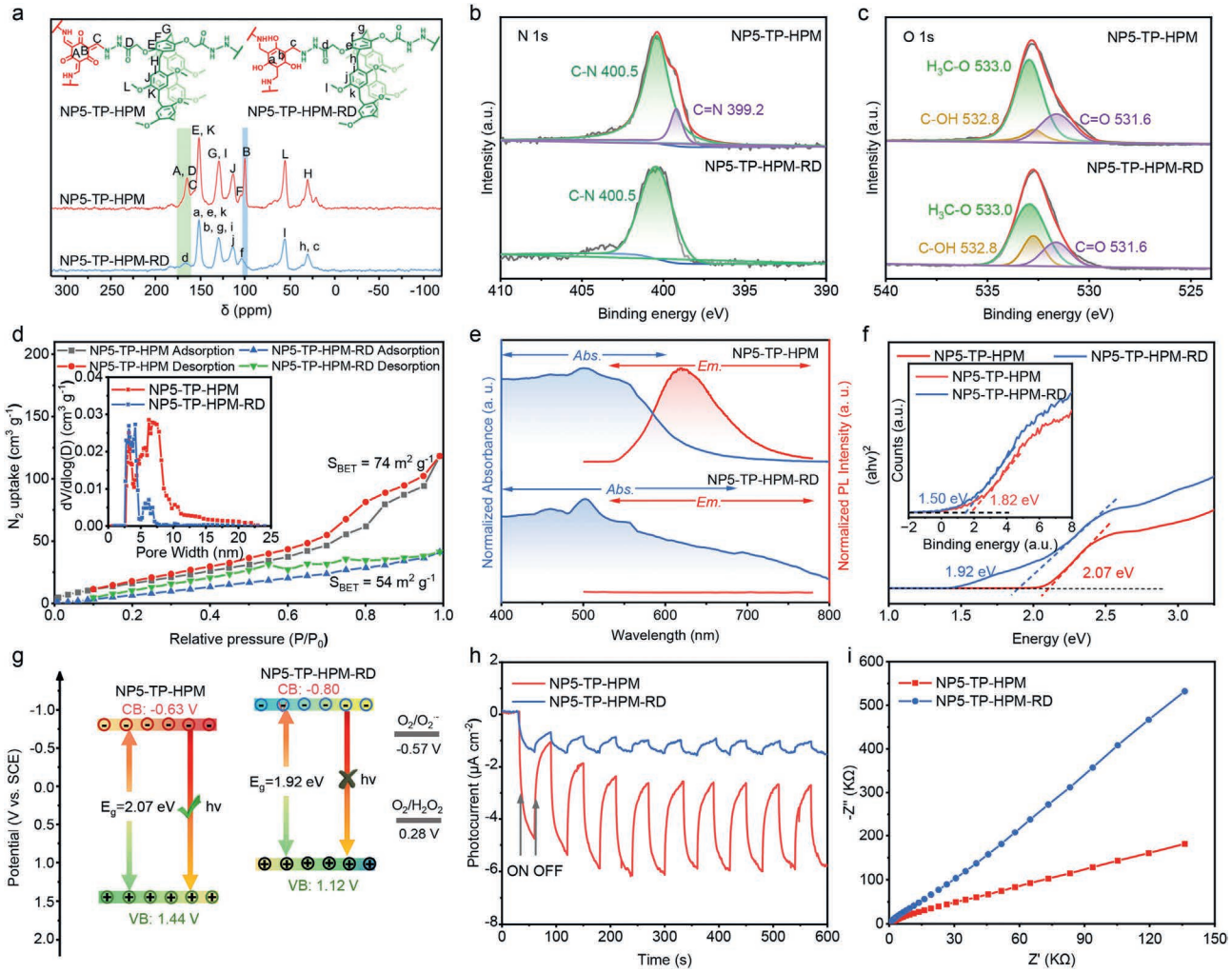


Fig. 2. (a) Solid-state ^{13}C NMR spectra of NP5-TP-HPM and NP5-TP-HPM-RD. (b) N 1s and (c) O 1s XPS spectra of NP5-TP-HPM and NP5-TP-HPM-RD. (d) N_2 absorption-desorption isotherms (77 K) of NP5-TP-HPM and NP5-TP-HPM-RD. Inset: Pore size distributions of NP5-TP-HPM and NP5-TP-HPM-RD. (e) UV–vis-DRS (blue lines) and PL (red lines) spectra of NP5-TP-HPM and NP5-TP-HPM-RD. (f) Direct optical band gaps of NP5-TP-HPM and NP5-TP-HPM-RD. Inset: Valence XPS spectra of NP5-TP-HPM and NP5-TP-HPM-RD. (g) Energy band positions of NP5-TP-HPM and NP5-TP-HPM-RD. (h) TPC curves and (i) EIS Nyquist plots of NP5-TP-HPM and NP5-TP-HPM-RD.

FT-IR spectrum of NP5-TP-HPM displayed characteristic signals at 3420, 1706, 1629, and 1206 cm^{-1}, corresponding to N–H, C=O, C=N, and C–N bonds, respectively, indicating complete hydrazone condensation. Upon $NaBH_4$ treatment, the C=N peak disappeared in the FT-IR spectrum of NP5-TP-HPM-RD, while the C–N peak persisted, confirming the reduction of the framework. Remarkably, concomitant with C=N reduction, the disappearance of the C=O peak and appearance of a broad 3020–3690 cm^{-1} band suggested the reduction of C=O groups to C–OH functionalities. Powder X-ray diffraction (PXRD) patterns revealed that NP5-TP-HPM and NP5-TP-HPM-RD exhibited amorphous structures (Fig. S2 in Supporting information), indicating that the reduction process did not substantially alter the framework topology. Furthermore, the reduction did not induce significant morphological changes, with both materials exhibiting solid microspheres (Fig. S3 in Supporting information).

Cross-polarization magic angle spinning (CP-MAS) nuclear magnetic resonance (NMR) spectroscopy further elucidated the structural relationship between NP5-TP-HPM and NP5-TP-HPM-RD (Fig. 2a). The ^{13}C NMR spectrum of NP5-TP-HPM exhibited characteristic resonances at 165, 55, and 30 ppm, corresponding to the carbon atoms of C=O groups (A, D), the $-OCH_3$ (L) of the pillar[5]arene side chain, and the $-CH_2-$ groups (H) of pillar[5]arene ring, respectively. Peaks at 100 and 158 ppm were attributed to the carbon atoms of the C=C bonds (B, C) in the β-ketoenamine structure of NP5-TP-HPM. This resonance-induced enol-keto tautomerization, facilitated by electron delocalization within the framework, is a characteristic feature observed in many enol-imine structural polymers [45]. Signals in the range of 105–151 ppm corresponded to the remaining aromatic carbon atoms (E, F, G, J, K, I). Upon reduction to NP5-TP-HPM-RD, the peak of the C=O carbon decreased and shifted, with the remaining signal (d) attributed to the carbon of the C=O band in the hydrazone linkage (green-shaded region). Notably, the disappearance of the C=C resonances from the β-ketoenamine structure suggests disruption of the enol-imine to keto-amine tautomerization pathway (blue-shaded region). This is likely a consequence of reduced conjugation and hindered electron delocalization upon reduction of the C=N bonds to C–N. Taken together, these data provide strong evidence for the successful synthesis of NP5-TP-HPM and NP5-TP-HPM-RD.

X-ray photoelectron spectroscopy (XPS) was employed to investigate the structural changes in the polymers. The N 1s XPS spectrum of NP5-TP-HPM exhibited two peaks at 400.5 and 399.2 eV (Fig. 2b), corresponding to C–N and C=N bonds, respectively. After reduction, the N 1s spectrum of NP5-TP-HPM-RD showed only a single peak at 400.5 eV, assigned to the C–N bond. The O 1s XPS spectrum of NP5-TP-HPM revealed peaks at 533.0, 532.8, and

531.6 eV (Fig. 2c), attributed to H_3C–O, C–OH, and C=O bonds, respectively. The relatively higher intensity of the C=O peak compared to that of C–OH suggested enol-keto tautomerization within the structure. While the O 1s XPS spectrum of NP5-TP-HPM-RD retained these peaks, the intensity of the C–OH signal increased substantially, reaching a magnitude comparable to that of the C=O peak. This suggests a significant presence of phenolic hydroxyl groups derived from the 2,4,6-triformylphloroglucinol building block, thus confirming the diminished enol-keto tautomerization after reduction. C 1s XPS spectra further corroborate this conclusion, revealing a significant increase in the C–OH level in NP5-TP-HPM-RD compared to NP5-TP-HPM (Fig. S4 in Supporting information). These findings have demonstrated that the reduction of C=N bonds within the 2,4,6-trihydroxybenzene-1,3,5-triimine units of NP5-TP-HPM by $NaBH_4$ effectively suppressed the phenol-to-quinone rearrangement of the framework, consistent with the solid-state ^{13}C NMR data.

Nitrogen adsorption-desorption isotherms were used to characterize the pore structure of NP5-TP-HPM and NP5-TP-HPM-RD (Fig. 2d). NP5-TP-HPM was characterized by a Brunner-Emmett-Teller surface area of 74 m^2/g, which decreased to 54 m^2/g upon reduction to NP5-TP-HPM-RD. Pore size analysis revealed that NP5-TP-HPM possesses a broad mesopore distribution, with maxima at approximately 3.1, 5.5, and 6.8 nm. In contrast, the pore sizes of NP5-TP-HPM-RD were predominantly distributed around 3.2 and 4.2 nm. The observed pore characteristics of NP5-TP-HPM are attributed to the loose interlayer packing resulting from the pillar-shaped cavities inherent in the framework. Furthermore, the heterogeneity in supramolecular organization, induced by the pillararenes, contributes to this phenomenon. The reduction process causes a decrease in surface area and a modification of the pore size distribution, suggesting increased backbone flexibility that results in partial pore occlusion. This may be attributed to diminished framework conjugation coupled with the development of attractive interactions between the electron-rich pillar[5]arene moieties and the flexible linker components. Thermogravimetric analysis revealed significant weight loss at 360 °C for NP5-TP-HPM and 335 °C for NP5-TP-HPM-RD, with 44 % and 56 % of the weight retained at 900 °C, respectively (Fig. S5 in Supporting information). Immersion of both materials in solutions of varying pH and organic solvents for 72 h, followed by FT-IR and PXRD analyses (Fig. S6 in Supporting information), confirmed structural and stacking integrity, indicating excellent chemical stability. Moreover, the FT-IR spectral changes observed for NP5-TP-HPM in HCl (aq., pH 1) and for NP5-TP-HPM-RD in NaOH (aq., pH 13) were attributed to enol-imine to keto-amine interconversion within the framework, induced by protonation of C=N bonds and deprotonation of -OH groups.

The optoelectronic properties of NP5-TP-HPM and NP5-TP-HPM-RD were investigated using UV–vis diffuse reflectance spectroscopy (UV–vis-DRS), photoluminescence (PL) spectroscopy, and electrochemical measurements. NP5-TP-HPM exhibited a broad absorption band from 400 nm to 630 nm, while NP5-TP-HPM-RD showed continuous absorption across the 400–800 nm range without a discernible absorption edge (Fig. 2e). Consistent with their absorption profiles, NP5-TP-HPM displayed PL emission between 540 and 780 nm, with a maximum at 630 nm (Fig. 2e). Conversely, NP5-TP-HPM-RD showed negligible fluorescence emission, correlating with its broad UV–vis absorption. Further analysis using the Kubelka-Munk function plot revealed band gaps of 2.07 and 1.92 eV for NP5-TP-HPM and NP5-TP-HPM-RD, respectively (Fig. 2f). Valence band XPS spectra directly measured valence band (VB) positions at 1.82 and 1.50 eV for NP5-TP-HPM and NP5-TP-HPM-RD, respectively, relative to the Fermi level (inset of Fig. 2f), corresponding to 1.44 and 1.12 V *vs.* the saturated calomel electrode (SCE) after conversion. Based on the equation $E_g = E_{VB} - E_{CB}$, the conduction band (CB) potentials were calculated to be −0.63 and −0.80 V, respectively (Fig. 2g). These values are in good agreement with the CB potentials of −0.69 and −0.84 V for NP5-TP-HPM and NP5-TP-HPM-RD derived from Mott-Schottky plots (Fig. S7 in Supporting information). Transient photocurrent (TPC) and electrochemical impedance spectroscopy (EIS) measurements revealed diminished photoelectronic response and charge transport capability for the reduced framework, NP5-TP-HPM-RD, compared to NP5-TP-HPM (Figs. 2h and i). This is likely due to a reduction in electron delocalization resulting from decreased conjugation.

Given the promising porosity, structural stability, and optoelectronic properties of these pillar[5]arene-based polymers, we investigated their photocatalytic performance at room temperature. Primary amines are crucial intermediates in organic synthesis, and their oxidative coupling to imines has garnered significant attention due to the widespread use of the resulting products in pharmaceuticals, agrochemicals, and dyes [53–56]. Consequently, we evaluated the photocatalytic activity of the pillar[5]arene-based frameworks using the oxidative coupling of benzylamine to *N*-benzyl-1-phenylmethanimine as a model reaction, demonstrating their potential for practical applications. Following reaction solvent optimization (Fig. S8 in Supporting information), NP5-TP-HPM and NP5-TP-HPM-RD achieved conversions of 99 % and 90 %, respectively, within 8 h (Fig. 3a), with NP5-TP-HPM reaching equilibrium after 4 h. The photocatalytic oxidation of benzylamine using NP5-TP-HPM proceeded at a rate of 10 mmol g^{-1} h^{-1}, which is 2.2-fold higher than that observed with NP5-TP-HPM-RD (4.5 mmol g^{-1} h^{-1}). To further validate the role of the pillar[5]arene in NP5-TP-HPM, a control polymer, NH-TP-COP, lacking the pillar[5]arene moiety, was synthesized (Fig. S9 in Supporting information). Its photocatalytic activity for benzylamine oxidative coupling was then evaluated under identical conditions. In O_2, NH-TP-COP afforded a yield of only 39 % after 1 h, significantly lower than that of NP5-TP-HPM (60 %). These results confirmed that the superior photocatalytic oxidation performance of NP5-TP-HPM arised from the pillar[5]arene cavity and framework connectivity. When benchmarked against representative systems in Table S1, NP5–TP–HPM lies near the upper end of reported mass–specific rates for covalent organic frameworks and is competitive with many metal–organic frameworks and metal oxides under their respective conditions (*e.g.*, PY–BDT COF, 7.92 mmol g^{-1} h^{-1}; BATA–BT COF, 5.58 mmol g^{-1} h^{-1}; PY–BDAT COF, 3.77 mmol g^{-1} h^{-1}; PCN–77, 1.52 mmol g^{-1} h^{-1}). Notably, it couples a high rate with near–quantitative conversion under our conditions, whereas many reported catalysts exhibit a trade-off between rate and conversion: some achieve high conversions only at lower rates (*e.g.*, TFPA–TPB–COF–Q, 7.14 mmol g^{-1} h^{-1} at 100 %; BTDA–TAPT, 5.56 mmol g^{-1} h^{-1} at ∼100 %; Zn–HOF, 0.83 mmol g^{-1} h^{-1} at 100 %), while others deliver moderate rates with reduced conversions (*e.g.*, CdS/Ag/$BiVO_4$, 6.17 mmol g^{-1} h^{-1} at 74 %; TA-COF-2, 6.67 mmol g^{-1} h^{-1} at 97 %). A few systems approach similar rates but with slightly lower conversions (*e.g.*, TA–COF–1, 10.0 mmol g^{-1} h^{-1} at 97 %).

To further elucidate the catalyst's crucial role in the reaction mechanism, control experiments were performed using NP5-TP-HPM, which displayed superior photocatalytic activity (Fig. 3b). In the absence of a photocatalyst or under dark conditions, benzylamine was not converted to *N*-benzyl-1-phenylmethanimine. Furthermore, the reaction conversion was significantly reduced under a N_2 atmosphere, yielding only 22 % *N*-benzyl-1-phenylmethanimine. These results demonstrate that NP5-TP-HPM can activate O_2 upon photoirradiation, thereby yielding ROS essential for the subsequent reaction, such as superoxide radical ($O_2^{\bullet-}$) and singlet oxygen ($^1O_2$). We further corroborated the above observations using electron paramagnetic resonance (EPR) spectroscopy. Upon light irradiation, the EPR spectra of NP5-TP-HPM exhibited signals corresponding to

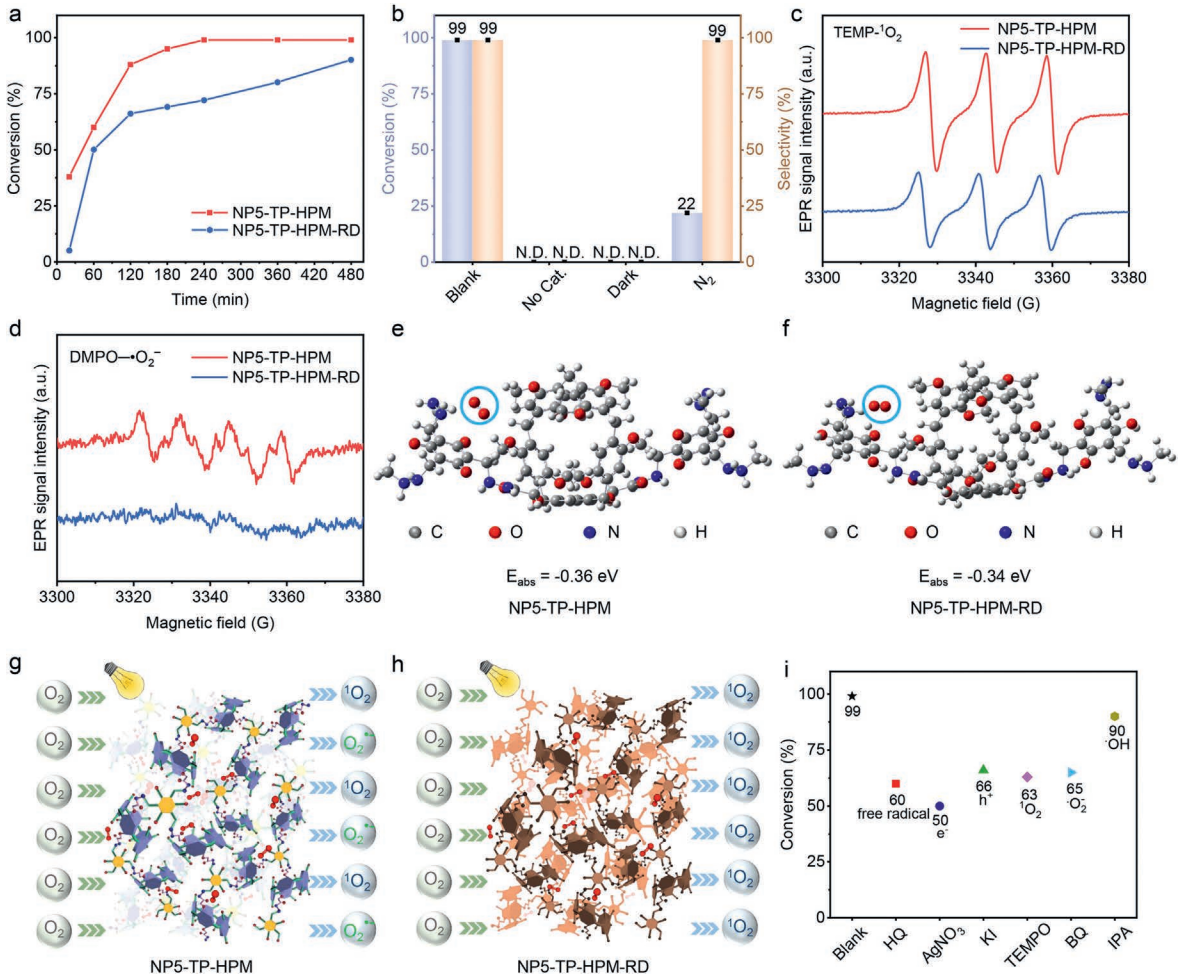


Fig. 3. (a) Kinetic profiles for the photocatalytic oxidative coupling of benzylamine using NP5-TP-HPM and NP5-TP-HPM-RD. (b) Screening of conditions for the photocatalytic oxidative coupling of benzylamine by NP5-TP-HPM. EPR spectra of (c) TEMP-$^1O_2$ and (d) DMPO-$O_2^{\bullet-}$ in the presence of NP5-TP-HPM and NP5-TP-HPM-RD under visible light irradiation. O_2 adsorption sites and configurations on (e) NP5-TP-HPM and (f) NP5-TP-HPM-RD. Schematic diagram of the photocatalytic generation of ROS by (g) NP5-TP-HPM and (h) NP5-TP-HPM-RD. (i) Effects of scavengers on trapping active species during the NP5-TP-HPM-photocatalyzed synthesis of *N*-benzyl-1-phenylmethanimine.

2,2,6,6-tetramethyl-4-piperidone (TEMP)-$^1O_2$ and 5,5-dimethyl-1-pyridine-*N*-oxide (DMPO)-$O_2^{\bullet-}$, whereas NP5-TP-HPM-RD showed only a weak signal for TEMP-$^1O_2$ (Figs. 3c and d).

Density functional theory (DFT) calculations were performed to elucidate the role of HPM in photocatalytic oxidation. These calculations probed the interaction energies between O_2 and the keto-enol structures, with a particular focus on variations in oxygen affinity. The results showed that the O_2 adsorption energy for NP5-TP-HPM (−0.36 eV) was more negative than that for NP5-TP-HPM-RD (−0.34 eV) (Figs. 3e and f), indicating a stronger interaction with O_2. This enhanced O_2 adsorption by NP5-TP-HPM is attributed to its β-ketoenamine moiety and the extended π-conjugation of the pillar[5]arene scaffold, which promotes significant π-electron delocalization. This, in turn, polarizes the electron cloud upon oxygen approach, fostering stronger dipole-dipole interactions. As a result, the differing photocatalytic oxidation activities of NP5-TP-HPM and NP5-TP-HPM-RD can be rationalized by the differences in their O_2 adsorption energies, which influence the nature and extent of ROS formed. Specifically, NP5-TP-HPM facilitates the concurrent generation of substantial quantities of both O_2 and $O_2^{\bullet-}$ (Fig. 3g), whereas NP5-TP-HPM-RD preferentially yields $^1O_2$ (Fig. 3h).

To further investigate the specific roles of electron/energy transfer in the reaction, trapping experiments were conducted (Fig. 3i). The conversion of benzylamine to *N*-benzyl-1-phenylmethanimine was significantly reduced to 60% upon addition of the radical scavenger hydroquinone (HQ), implying the participation of various radicals, such as benzylamine radical cations and $O_2^{\bullet-}$. The introduction of a hole scavenger (KI) and an electron scavenger ($AgNO_3$) reduced the conversion to 50% and 66%, respectively. Furthermore, scavenging of $^1O_2$ and $O_2^{\bullet-}$ with 2,2,6,6-tetramethylpiperidine-1-oxyl (TEMPO) and benzoquinone (BQ), respectively, resulted in conversions of 63% and 65%. Conversely, the addition of isopropanol (IPA), a hydroxyl radical ($^{\bullet}OH$) scavenger, only slightly inhibited the conversion, resulting in a conversion of approximately 90%. These findings suggest that, upon irradiation, NP5-TP-HPM is excited, generating electron-hole pairs, which can then obtain electrons from benzylamines, generating active cation radicals, and transfer electrons and energy to adsorbed O_2, yielding active $O_2^{\bullet-}$ and $^1O_2$ species.

The preceding results suggest a dual-pathway mechanism for the photocatalytic benzylamine coupling reaction [42,57], involving hole-dominated activation coupled with ROS-mediated oxidation (Fig. S10 in Supporting information). Upon light irradiation, NP5-TP-HPM absorbed photon energy, promoting electrons from the VB to the CB and generating electron-hole pairs. The holes oxidized benzylamine at the catalyst surface, forming a benzylamine radical cation A ($PhCH_2NH^{\bullet+}$). This intermediate subsequently reacted with $^1O_2$ generated by holes and $O_2^{\bullet-}$ activated by electrons, both pathways accelerating the formation of the imine interme-

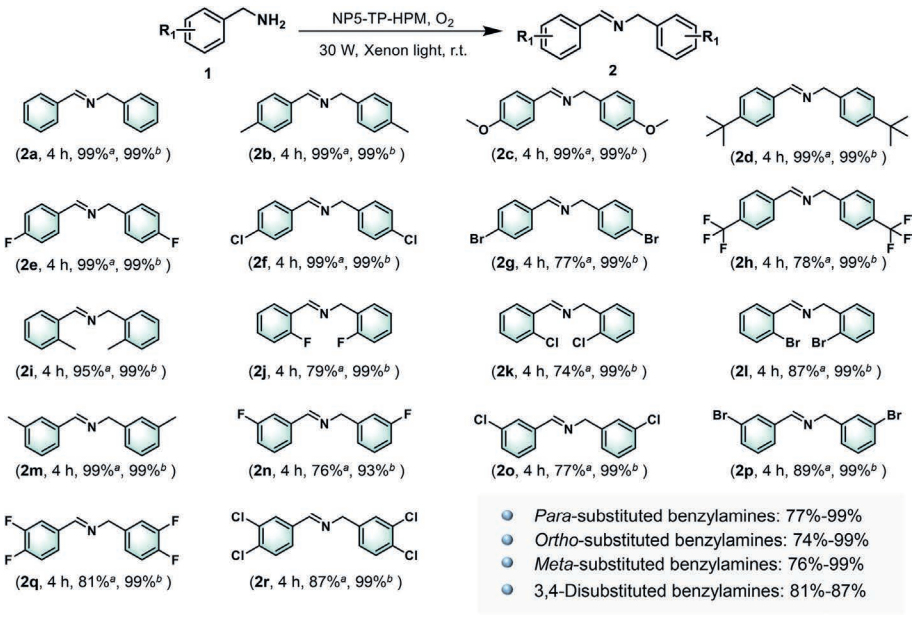


Fig. 4. Scope of the photocatalytic oxidation coupling reaction. Reaction conditions: 0.2 mmol of substrates, 5 mg of photocatalyst (NP5-TP-HPM), 2 mL of CH_3CN, irradiated by 300 W Xenon light with 420 nm filter, determined by ^1H NMR analysis. [a] Conversion. [b] Selectivity.

diate B (PhCH-NH). The PhCH-NH can undergo nucleophilic addition by benzylamine to form intermediate C, followed by elimination of ammonia (NH_3) to yield *N*-benzyl-1-phenylmethanimine. In parallel, PhCH-NH can further undergo dehydrogenation and oxidation to form benzaldehyde, which then reacts with benzylamine *via* nucleophilic addition and dehydration, yielding *N*-benzyl-1-phenylmethanimine. After four catalytic cycles, NP5-TP-HPM retained >90% conversion to *N*-benzyl-1-phenylmethanimine (Fig. S11 in Supporting information). Furthermore, catalyst removal after 1 h of irradiation resulted in no significant increase in conversion after an additional 7 h (Fig. S12 in Supporting information), confirming the necessity of the catalyst and ruling out catalyst leaching or degradation. FT-IR and XRD analyses revealed no structural or packing changes in NP5-TP-HPM before and after catalysis (Fig. S13 in Supporting information). These findings demonstrate NP5-TP-HPM to be an efficient and robust heterogeneous photocatalyst.

Encouraged by these findings, we systematically investigated the versatility of NP5-TP-HPM for the photocatalytic oxidative synthesis of imine derivatives (Fig. 4). Benzylamines bearing electron-donating or electron-withdrawing groups at the *para*-position were converted to the corresponding imines in high conversions (77%–99%) within 4 h (**2a**-**2h**). Similarly, *ortho*-substituted benzylamines were also efficiently converted to the corresponding imines with conversions of 74%–95% (**2i**-**2l**). Furthermore, *meta*-substituted benzylamines underwent oxidative coupling with comparable efficiency (**2m**-**2p**, 76%–99%). Despite the anticipated inhibitory effect of electron-withdrawing groups on $PhCH_2NH^{\bullet+}$ radical formation, NP5-TP-HPM facilitated the efficient transformation of these substrates, affording the corresponding imines in conversions of 74%–99% (**2e**–**2h**, **2j**–**2l**, **2n**–**2p**). This is further exemplified by the successful conversion of substrates bearing multiple electron-withdrawing substituents to the desired imines in yields of 81% and 87% using NP5-TP-HPM (**2q**, **2r**). Bulky substituents on the benzylamine moiety only slightly diminished the photocatalytic oxidative coupling proficiency of NP5-TP-HPM (**2d**, **2l**, **2p**; 99%, 87%, 89%).

To elucidate the origin of the observed high efficiency, we conducted a detailed spectroscopic investigation, employing ^1H NMR to probe the function of the pillararene moiety. The methylene protons of benzylamine exhibited an upfield chemical shift from 3.87 ppm to 3.77 ppm upon encapsulation within the pillararene cavities (Fig. S14 in Supporting information), indicating the host–guest interactions between the electron-rich pillararene and the benzylamine. This interaction facilitates the confinement and aggregation of benzylamine molecules within the pillararene cavities, thereby promoting the photoactivation of the substrate. Furthermore, DFT calculations were employed to elucidate the role of the pillar[5]arene moiety within the framework. Electrostatic potential analysis revealed a significant accumulation of electron density localized within the pillar[5]arene cavities of both NP5-TP-HPM and NP5-TP-HPM-RD networks (Fig. 5a). This observation suggests that the cavity's geometry and electronic properties can exhibit an affinity for electron-deficient substrates, specifically benzylamine radical cations, effectively reducing the distance required for their interaction with $^1O_2$ and $O_2^{\bullet-}$, and thereby accelerating the catalytic oxidation process. Moreover, the pillar[5]arene cavities in NP5-TP-HPM-RD exhibited a higher electron density compared to those in NP5-TP-HPM, indicating that reduction of the framework leads to a greater accumulation of electrons within the cavities, further amplifying their electron-rich character. This amplified electron density provides a theoretical basis for the enhanced adsorption of cationic pollutants subsequently observed in NP5-TP-HPM-RD.

Beyond photocatalysis, adsorption also represents a crucial application in practical scenarios [31,58–64]. The widespread use of organic dyes in textiles, cosmetics, printing, and thermoplastics underscores the urgent need for the development of efficient dye-adsorbing materials [31,65–68]. Therefore, we further investigated the adsorption behavior of NP5-TP-HPM and NP5-TP-HPM-RD towards RhB. Upon addition of 10 mg of each polymer to 20 mL of a 150 mg/L RhB solution, NP5-TP-HPM-RD exhibited a RhB removal efficiency of 95% after 40 h, while NP5-TP-HPM achieved only 69% (Fig. 5b and Fig. S15 in Supporting information). Adsorption kinetic studies of RhB onto NP5-TP-HPM and NP5-TP-HPM-RD revealed that the data for both materials exhibited excellent fitting to the *pseudo*-second-order kinetic model ($R^2 = 0.999$) (Fig. 5c). This strongly suggests that the adsorption process is primarily governed by chemical adsorption, with physical interactions playing a secondary role. Consequently, the adsorption capacity is dictated by

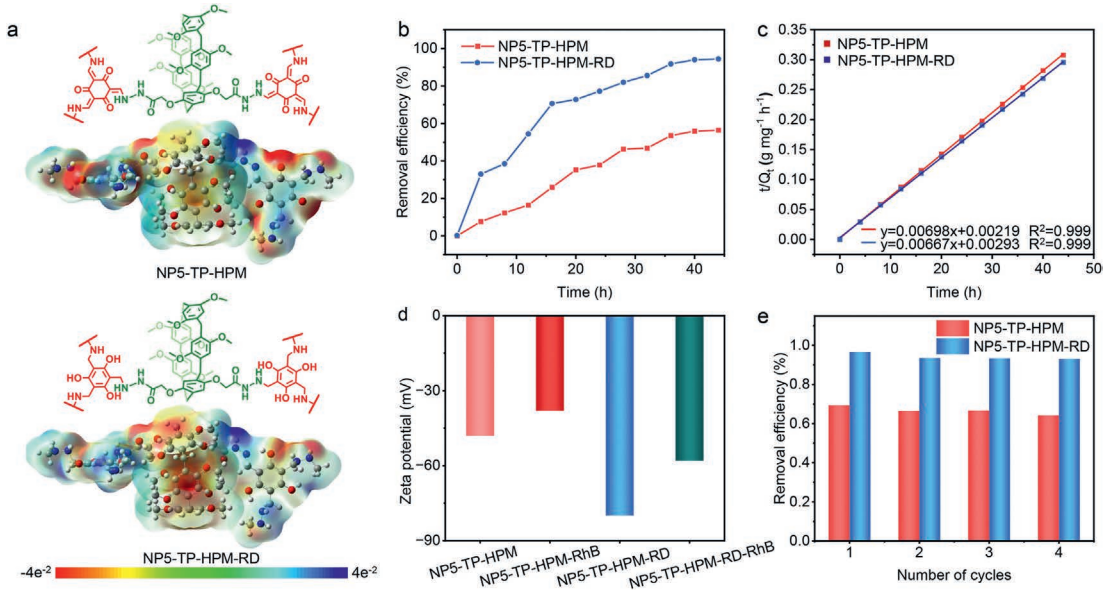


Fig. 5. (a) Electrostatic potential profiles of the repeating fragments of NP5-TP-HPM and NP5-TP-HPM-RD. (b) RhB removal efficiency from water by NP5-TP-HPM and NP5-TP-HPM-RD. Conditions: RhB (150 mg/L), adsorbent (0.5 mg/mL). (c) Fitting of the pseudo-second-order kinetic model to the experimental data for the adsorption of RhB by NP5-TP-HPM and NP5-TP-HPM-RD. (d) Zeta potential of NP5-TP-HPM, NP5-TP-HPM-RhB, NP5-TP-HPM-RD, and NP5-TP-HPM-RD-RhB. (e) Recyclability of NP5-TP-HPM and NP5-TP-HPM-RD for RhB adsorption over four cycles.

both the strength of the interactions and the number of specific adsorption sites available on the adsorbent surface [69,70]. Furthermore, the calculated equilibrium adsorption capacity of NP5-TP-HPM-RD for RhB was 150 mg/g, significantly surpassing the performance of numerous other adsorbents reported in the literature (Fig. S16 in Supporting information).

To elucidate the enhanced RhB adsorption of NP5-TP-HPM-RD compared to NP5-TP-HPM, zeta potential and hydrophilicity measurements were conducted. NP5-TP-HPM and NP5-TP-HPM-RD exhibited zeta potentials of −47 and −79 mV, respectively. Upon RhB adsorption, these values shifted to −37 and −57 mV (Fig. 5d), indicating stronger electrostatic interactions between NP5-TP-HPM-RD and the cationic dye RhB. The negative zeta potentials of both materials primarily originate from the pillar[5]arene units and imine linkages, with the more negative potential of NP5-TP-HPM-RD attributed to lone pair electrons generated upon reduction of C=N to C–N bonds. Thus, the superior RhB adsorption capacity of NP5-TP-HPM-RD stems from the abundance of negatively charged sites, exhibiting a strong affinity for the cationic dye. Beyond electrostatic attraction, FT-IR spectra of NP5-TP-HPM-RhB and NP5-TP-HPM-RD-RhB revealed broad peaks around 3430 and 3427 cm^{-1} (Fig. S17 in Supporting information), respectively. These peaks represented a shift of 18 and 57 cm^{-1} compared to the corresponding peaks of NP5-TP-HPM and NP5-TP-HPM-RD at 3412 and 3370 cm^{-1}, indicative of hydrogen bonding interactions between the frameworks and RhB. The higher concentration of -C-NH- and -OH groups in NP5-TP-HPM-RD compared to NP5-TP-HPM provides more opportunities for hydrogen bonding with heteroatoms in RhB. This can be further supported by water contact angle measurements, which show a decrease in the contact angle from 145° to 110° upon reduction, indicating an increase in hydrophilicity (Fig. S18 in Supporting information). Furthermore, NP5-TP-HPM-RD demonstrated good cycling stability, retaining a RhB removal efficiency of 93 % after four cycles, significantly higher than the 67 % observed for NP5-TP-HPM (Fig. 5e and Fig. S19 in Supporting information). FT-IR and SEM analyses confirmed the structural and morphological integrity of the material after cycling (Figs. S20 and S21 in Supporting information), suggesting its potential as an efficient adsorbent for practical applications.

In summary, we have successfully synthesized hydrazone-linked pillar[5]arene-based macrocycle polymers *via* a bottom-up networking strategy, generating efficient photocatalysts. Reduction of these polymers yielded adsorbents with remarkable capacity for cationic dye removal. The inherent electron-rich cavities of the pillar[5]arenes drive this functionality, optimizing photophysical and photochemical properties through optoelectronic characteristics and enabling strong electrostatic interactions with cationic compounds. In photocatalysis, the polymers exhibit sensitive photoresponsiveness and efficient photoelectron transfer while simultaneously attracting benzylamines and aminium radical cations *via* confinement effects. This proximity effect reduces the electron transfer distance from the catalyst to the substrate (reactive intermediate), enabling highly efficient, confined photocatalysis for the oxidative coupling of benzylamine and its derivatives, achieving conversions ranging from 74 % to 99 %. For adsorption, the electron-rich nature of the pillar[5]arene cavities within the reduced HPM is further amplified, effectively removing cationic dye RhB through electrostatic attraction and hydrogen bonding with N–H and –OH groups. This work highlights the crucial role of supramolecular macrocyclic arenes, particularly pillar[*n*]arenes, in sustainable applications such as catalysis and adsorption. We envisage that these pillar[*n*]arene-based covalent organic polymers hold significant promise for enhancing energy efficiency and promoting the utilization of renewable energy sources.

Declaration of competing interest

The author is an Editorial Board Member/Editor-in-Chief/Associate Editor/Guest Editor for this journal and was not involved in the editorial review or the decision to publish this article.

CRediT authorship contribution statement

Meng-Hao Li: Writing – original draft, Investigation, Formal analysis, Data curation, Conceptualization. **Hui Hui:** Writing – original draft, Formal analysis, Data curation. **Yan Wang:** Validation,

Supervision, Resources, Project administration. **Weiwei Huan:** Validation, Supervision, Resources, Project administration, Funding acquisition. **Ying-Wei Yang:** Writing – review & editing, Validation, Supervision, Project administration, Funding acquisition, Formal analysis, Conceptualization.

Acknowledgments

The authors acknowledge the National Natural Science Foundation of China (No. 22571119) and the Fundamental Research Funds for the Central Universities (No. 2025-JCXK-24) for financial support.

Supplementary materials

Supplementary material associated with this article can be found, in the online version, at doi:10.1016/j.cclet.2025.112016.

References

[1] Z. Liu, S.K.M. Nalluri, J.F. Stoddart, Chem. Soc. Rev. 46 (2017) 2459–2478.
[2] X. Ma, Y. Zhao, Chem. Rev. 115 (2015) 7794–7839.
[3] R. Kumar, A. Sharma, H. Singh, et al., Chem. Rev. 119 (2019) 9657–9721.
[4] X. Li, M. Shen, J. Yang, et al., Adv. Mater. 36 (2024) 2313317.
[5] K. Zhang, X.Y. Lou, Y. Wang, et al., Chin. Chem. Lett. 36 (2025) 110464.
[6] X.N. Han, Y. Han, C.F. Chen, Chem. Soc. Rev. 52 (2023) 3265–3298.
[7] H. Zhu, L. Chen, B. Sun, et al., Nat. Rev. Chem. 7 (2023) 768–782.
[8] J.R. Wu, Y.W. Yang, Angew. Chem. Int. Ed. 60 (2021) 1690–1701.
[9] Y. Wu, M. Tang, M.L. Barsoum, et al., Chem. Soc. Rev. 54 (2025) 2906–2947.
[10] Y. Li, X. Lou, C. Wang, et al., Chin. Chem. Lett. 34 (2023) 107877.
[11] C.Y. Wang, Y.Q. Liu, C. Jia, et al., Chin. Chem. Lett. 34 (2023) 108400.
[12] Z.Q. Wang, X. Wang, Y.W. Yang, Adv. Mater. 36 (2024) 2301721.
[13] M. Xue, Y. Yang, X. Chi, et al., Acc. Chem. Res. 45 (2012) 1294–1308.
[14] J. Yang, X.Y. Lou, D. Dai, et al., Chin. Chem. Lett. 36 (2025) 109818.
[15] C.M. Kane, O. Ugono, L.J. Barbour, et al., Chem. Mater. 27 (2015) 7337–7354.
[16] Y. Zhou, K. Jie, R. Zhao, et al., J. Am. Chem. Soc. 141 (2019) 11847–11851.
[17] Z. Li, Z. Yang, Y. Zhang, et al., Angew. Chem. Int. Ed. 61 (2022) e202206144.
[18] W. Chen, P. Chen, G. Zhang, et al., Chem. Soc. Rev. 50 (2021) 11684–11714.
[19] Z. Li, Y.W. Yang, Adv. Mater. 34 (2022) 2107401.
[20] T. Skorjanc, D. Shetty, A. Trabolsi, Chem 7 (2021) 882–918.
[21] D. Xia, P. Wang, X. Ji, et al., Chem. Rev. 120 (2020) 6070–6123.
[22] S.B. Yu, F. Lin, J. Tian, et al., Chem. Soc. Rev. 51 (2022) 434–449.
[23] Q. Sun, B. Aguila, S. Ma, Trends Chem. 1 (2019) 292–303.
[24] K.S. Song, P.W. Fritz, A. Coskun, Chem. Soc. Rev. 51 (2022) 9831–9852.
[25] J. Yang, H. Xu, J. Li, et al., Science 385 (2024) 1115–1120.
[26] L. Liu, Z. Liu, J. Cui, et al., Chin. Chem. Lett. 35 (2024) 108422.
[27] Y. Zhang, S.N. Riduan, Chem. Soc. Rev. 41 (2012) 2083–2094.
[28] M. Debruyne, V. Van Speybroeck, P. Van Der Voort, et al., Green Chem. 23 (2021) 7361–7434.
[29] X. Liu, C.F. Liu, S. Xu, et al., Chem. Soc. Rev. 51 (2022) 3181–3225.
[30] N. Singh, S. Son, J. An, et al., Chem. Soc. Rev. 50 (2021) 12883–12896.
[31] Y. Song, J. Phipps, C. Zhu, et al., Angew. Chem. Int. Ed. 62 (2023) e202216724.
[32] J.S.M. Lee, A.I. Cooper, Chem. Rev. 120 (2020) 2171–2214.
[33] X. Wang, X. Ding, Y. Jin, et al., Angew. Chem. Int. Ed. 62 (2023) e202302808.
[34] I. Ahmed, H.J. Lee, S.H. Jhung, Chem. Eng. J. 499 (2024) 156148.
[35] S. Karak, K. Koner, A. Karmakar, et al., Adv. Mater. 36 (2024) 2209919.
[36] J. Xu, G. Feng, D. Ao, et al., Adv. Mater. 36 (2024) 2406256.
[37] M.H. Li, Z. Yang, H. Hui, et al., Nano Lett. 25 (2025) 7524–7532.
[38] C. Sun, D. Sheng, B. Wang, et al., Angew. Chem. Int. Ed. 62 (2023) e202303378.
[39] L. Ou, Z. Xue, B. Li, et al., Chin. Chem. Lett. 36 (2025) 110294.
[40] Y. Zhang, J. Duan, D. Ma, et al., Angew. Chem. Int. Ed. 56 (2017) 16313–16317.
[41] M.H. Li, C. Xu, Y.W. Yang, Coord. Chem. Rev. 512 (2024) 215894.
[42] M.H. Li, Z. Yang, Z. Li, et al., Chem. Mater. 34 (2022) 5726–5739.
[43] Z.Q. Wang, M.H. Li, S. Liang, et al., J. Am. Chem. Soc. 147 (2025) 13618–13628.
[44] L. Liu, Y. Hu, S. Huang, et al., Chem. Sci. 12 (2021) 13316–13320.
[45] Y. Yuan, K.T. Bang, R. Wang, et al., Adv. Mater. 35 (2023) 2210952.
[46] K. Jie, Y. Zhou, Q. Sun, et al., Nat. Commun. 11 (2020) 1086.
[47] P. Wu, Y. Qi, Q. Li, et al., ACS Sustain. Chem. Eng. 11 (2023) 502–513.
[48] S.N. Talapaneni, D. Kim, G. Barin, et al., Chem. Mater. 28 (2016) 4460–4466.
[49] D. Dai, J. Yang, Y.C. Zou, et al., Angew. Chem. Int. Ed. 60 (2021) 8967–8975.
[50] M.H. Li, Z. Yang, H. Hui, et al., Angew. Chem. Int. Ed. 62 (2023) e202313358.
[51] D. Zhen, C. Liu, Q. Deng, et al., Chin. Chem. Lett. 35 (2024) 109249.
[52] F. Chu, G. Hai, D. Zhao, et al., ACS Catal. 13 (2023) 13167–13180.
[53] Y. Xu, Y. Chen, W.F. Fu, Appl. Catal. B: Environ. 236 (2018) 176–183.
[54] S.I. Naya, K. Kimura, H. Tada, ACS Catal. 3 (2013) 10–13.
[55] B. Chen, L. Wang, S. Gao, ACS Catal. 5 (2015) 5851–5876.
[56] X. Wang, M. Cheng, Y. Liu, et al., Inorg. Chem. 64 (2025) 11561–11570.
[57] M.Y. Yang, S.B. Zhang, M. Zhang, et al., J. Am. Chem. Soc. 146 (2024) 3396–3404.
[58] X. Liu, Y. Shan, S. Zhang, et al., Green Energy Environ. 8 (2023) 698–721.
[59] A.M. Awad, S.M.R. Shaikh, R. Jalab, et al., Sep. Purif. Technol. 228 (2019) 115719.
[60] I. Ahmed, S.H. Jhung, Chem. Eng. J. 310 (2017) 197–215.
[61] C. Bao, C.L. Fang, Water Resour. Manage. 26 (2012) 531–552.
[62] L. Zhu, D. Shen, K.H. Luo, J. Hazard. Mater. 389 (2020) 122102.
[63] Z. Lv, C. Wang, W. Liu, et al., Adv. Energy Mater. 14 (2024) 2402551.
[64] G. Wu, J.R. Wu, Y. Wang, et al., Chem 9 (2023) 2918–2930.
[65] Y. Chen, S.R. Zhai, N. Liu, et al., Bioresour. Technol. 144 (2013) 401–409.
[66] D. Jiang, M. Chen, H. Wang, et al., Coord. Chem. Rev. 380 (2019) 471–483.
[67] Z.M. Şenol, N. El Messaoudi, Z. Ciğeroglu, et al., Food Chem. 450 (2024) 139398.
[68] B. Garai, D. Shetty, T. Skorjanc, et al., J. Am. Chem. Soc. 143 (2021) 3407–3415.
[69] C.L. Song, M.H. Li, G. Wu, et al., ACS Mater. Lett. 7 (2025) 1905–1913.
[70] Y. Hou, A. Jia, X. Qin, et al., Environ. Pollut. 340 (2024) 122659.